NJC

ROYAL SOCIETY OF CHEMISTRY

PAPER

View Article Online
View Journal | View Issue

Cite this: *New J. Chem.*, 2025, 49, 5330

Diagnosing the role of hydrogen bonding in the organization, aggregation, and optical properties of phthalhydrazide-functionalized molecules in solution and solid state†‡

Cheng-Yen Pan,§[a] Nathan J. Grinalds,§[b] Ion Ghiviriga,[a] Khalil A. Abboud,[a] Jiangeng Xue*[b] and Ronald K. Castellano *[a]

To realize optoelectronics based on self-assembling organic semiconductors, it is imperative to have both excellent molecular design and conditions that facilitate well-behaved molecular assembly. We previously reported how hydrogen-bond (HB)-directed self-assembly of π-conjugated donor materials with a phthalhydrazide (PH) functional group can improve active layer morphology and charge transport in organic photovoltaics (OPVs). In this work, we improved the molecular design by synthesizing new hydrogen-bonding (H-bonding) capable molecules featuring narrower optical gaps and enhanced solubility. We evaluated their self-assembling properties in a variety of environments (solvents, temperatures, concentrations, *etc.*) and in the solid state to establish procedures to prepare films with predictable structural and optical properties. The new H-bonding molecules (**iQPH** and **iQPH-BO**) and their comparator compounds (**QPMe** and **QPMe-BO**) were prepared by fusing a phthalhydrazide unit and quinoxaline unit to achieve donor–acceptor functionality. By characterizing **iQPH** in solution using ultraviolet-visible (UV-vis) spectroscopy, nuclear magnetic resonance (NMR) methods, density functional theory (DFT), and single crystal X-ray diffraction, we discovered its surprisingly complex structural, self-assembling, and optical properties. Thin film structural characterization by atomic force microscopy (AFM) and grazing-incidence wide-angle X-ray scattering (GIWAXS) revealed "locked-in" morphology and superior thermal stability in **iQPH-BO** films compared to **QPMe-BO** films due to H-bonded supramolecular assemblies. Negligible changes in UV-vis absorption were observed for **iQPH-BO** films even when annealed at temperatures over 150 °C. This work supports the idea that H-bonding compounds can effectively control the morphology of photoactive layers and enhance the robustness of optoelectronic devices. This work also underscores the complexity of using H-bonding to mediate the self-assembly of π-conjugated small molecule compounds. In doing so, we contribute to the growing body of molecular design principles aimed at achieving programmable supramolecular assemblies in organic optoelectronics.

Received 29th December 2024,
Accepted 13th February 2025

DOI: 10.1039/d4nj05529b

rsc.li/njc

Introduction

The self-assembly of π-conjugated compounds into programmable structures has been a longstanding desire of chemists with materials scientists eager to integrate them into novel devices. In recent decades, the design rules and strategies to achieve programmable solid-state structures from organic compounds in solution have advanced significantly.[1–5] While traditional π-conjugated polymers and oligomers have paved the way for significant breakthroughs in optoelectronics, they often face challenges such as limited solubility, morphological instability, and batch-to-batch variation.[6–8] Self-assembling π-conjugated small molecules offer unique advantages over their polymeric counterparts including higher crystallinity, charge carrier mobility, and programmable morphology.[9,10]

Extensive efforts have been made towards optimizing the morphology in organic optoelectronic devices. These strategies mainly focus on post-synthesis processing efforts such as solvent annealing,[11,12] thermal annealing,[13–16] and the inclusion of active layer additives (*e.g.*, 1,8-diiodooctane, chloronapthalene).[17–19] Unfortunately, these techniques still result in unpredictable

[a] *Department of Chemistry, University of Florida, PO Box 117200, Gainesville, FL 32611, USA. E-mail: castellano@chem.ufl.edu*
[b] *Department of Materials Science and Engineering, University of Florida, PO Box 116400, Gainesville, FL 32611, USA. E-mail: jxue@mse.ufl.edu*

† Dedicated to Prof. Dr Frank Würthner on the occasion of his 60th birthday.

‡ Electronic supplementary information (ESI) available. CCDC 2390133. For ESI and crystallographic data in CIF or other electronic format see DOI: https://doi.org/10.1039/d4nj05529b

§ Authors contributed equally.

nanoscale morphology and require intensive optimization through trial and error. These concerns are particularly relevant to the photoactive layers of organic photovoltaics (OPVs) that utilize the bulk heterojunction (BHJ) architecture and require multiple annealing steps during device fabrication.[6] Device performance and active layer morphology are often initially enhanced after annealing due to more ideal phase separation of donor and acceptor materials which balances exciton dissociation and charge transport.[6,20–23] However, the tendency of small molecules and polymers to undergo further structural changes during thermal processing and operation is typically detrimental to the power conversion efficiency (PCE) and stability of the device over prolonged periods of time.[24] The inability to fabricate devices with stable performance has hindered the organic electronics community for a long time.[25,26] It is necessary, therefore, to develop materials that maintain their solid-state structures immediately after their deposition and maintain their intended morphology after the moderate heat exposure that would be experienced in realistic manufacturing and operational settings.

Supramolecular assembly provides a route to control morphology issues and thermal stability from a "bottom-up" perspective. Functional groups can be pre-installed onto molecules to direct molecular assembly which makes the molecular packing and distribution more consistent and robust, providing a promising and reliable avenue to improve active layer morphology.[27] In particular, functional groups with hydrogen bonding (H-bonding) capabilities allow molecules to arrange into stable and well-organized assemblies and are promising candidates to this end.[28–33]

Phthalhydrazide (PH) has been known to form trimeric rosettes with H-bonding interactions through lactam–lactim tautomerization in the solid and liquid states which imparts PH-functionalized materials one-dimensional organization and enhanced thermal stability.[28–30] The self-assembling and rosette-forming capability of the PH group has been studied with various substituents such as alkyl and alkoxy chains,[28,30] crown ethers,[31] helicenes,[29] and oligothiophenes (Fig. 1).[32–35]

In previously published work, we reported a systematic structure–property relationship study to demonstrate how an H-bonding functional group improved molecular packing and PCE in vacuum-deposited OPV devices.[32,35] The donor materials in the previous study were based on branched and linear

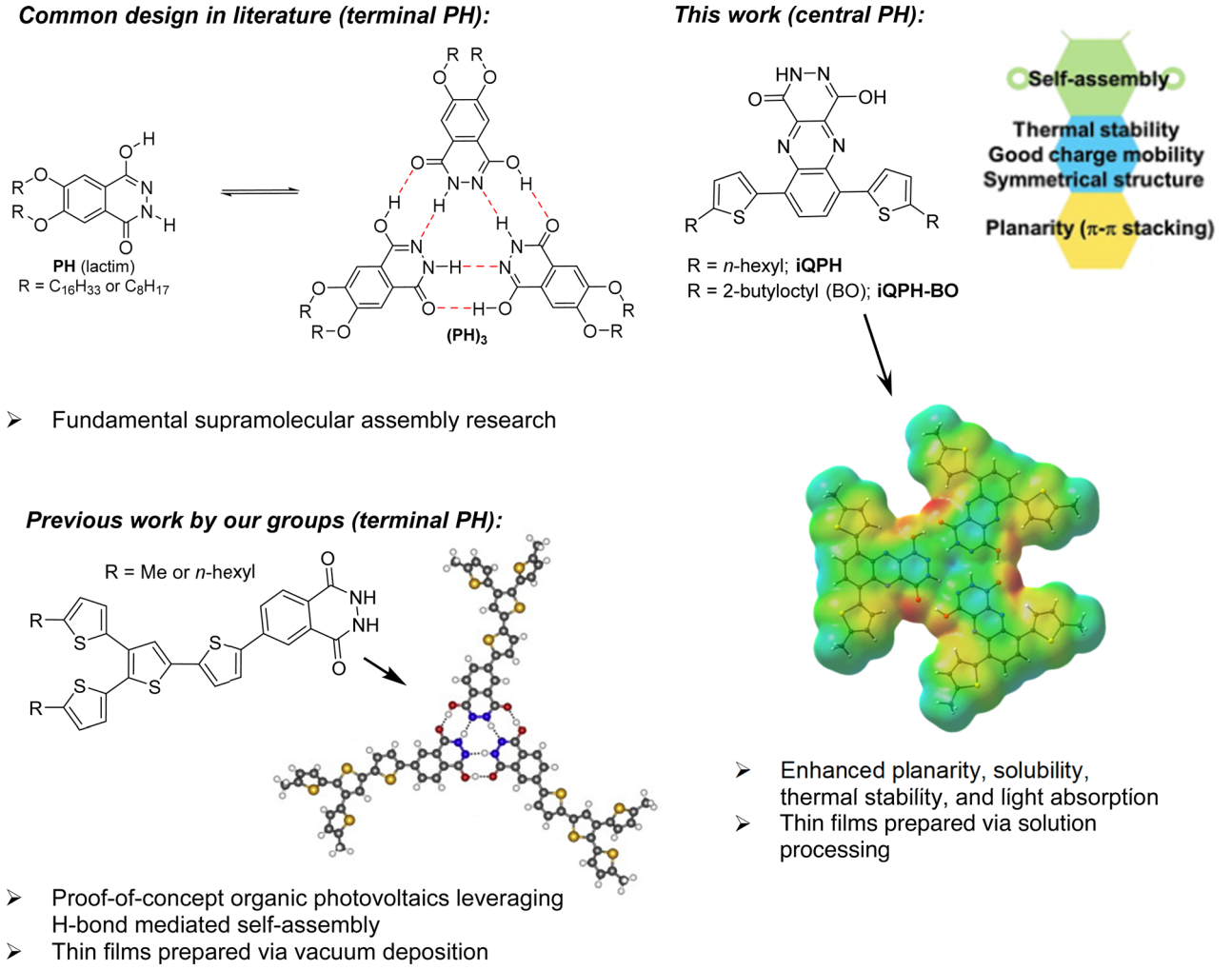

Fig. 1 Molecular structures of phthalhydrazide (PH) containing compounds that are capable of self-assembling into trimeric structures.

quarterthiophenes functionalized with PH heterocycles that enabled self-complementary H-bonding interactions. Two sets of structurally and optoelectronically similar molecules were synthesized, with the only difference being their H-bonding capability. The PH unit in the H-bonding capable material facilitated vertical charge transport relative to the substrate, enhanced charge collection length, and better solar energy utilization. With these advantages, the OPVs with the H-bonding capable material had double the PCE compared to devices with the H-bonding incapable comparators with minimal change in the open-circuit voltage (V_{oc}). Scanning tunneling microscopy studies on Au (111) also verified the formation of stable trimer rosettes, which rationalized the improved photovoltaic performance of the BHJ cells and verified the success of the molecular design (Fig. 1).

To harness the potential of high throughput (and low-cost) solution processing of organic materials, we shifted focus on developing H-bonding capable compounds with enhanced solubility to avoid having to rely on vacuum deposition. Efforts were made to synthesize compounds that possessed both extensive conjugation and H-bonding capabilities since the PH-functionalization reduces solubility significantly which is problematic during synthesis and purification. By migrating the PH group from the terminus to a centralized position (with respect to the conjugated side units), we achieved a highly planar structure that we hypothesized would offer better supramolecular organization compared to previous works, and with proper alkyl chain functionalization, could achieve solubilities up to *ca.* 20 mg mL^{-1} in solvents such as chloroform and toluene (Fig. 1). This molecular design is also motivated by the desire to balance the interplay between H-bonding mediated assembly and the competing π–π interactions of the conjugated side units which can hinder trimer formation.

The new H-bonding molecules (**iQPH** and **iQPH-BO**) and their comparator compounds (**QPMe** and **QPMe-BO**) were prepared by fusing a phthalhydrazide unit and quinoxaline unit to achieve donor–acceptor functionality (Scheme 1). With improved molecular design bestowing narrower optical gaps and enhanced solubility, we evaluated the self-assembling properties of the model compounds in a variety of solution conditions (varying solvents, temperatures, concentrations, *etc.*) and in the solid state to establish recipes for preparing films with predictable structural and optical properties. By characterizing **iQPH** in solution using ultraviolet-visible (UV-vis) spectroscopy, nuclear magnetic resonance (NMR) methods, density functional theory (DFT), and single crystal X-ray diffraction, we discovered its surprisingly complex structural, self-assembly, and optical properties. Solid-state characterization of these materials revealed intriguing morphological and optoelectronic differences associated with the presence or lack of hydrogen bonding. Structural characterization by atomic force microscopy (AFM) and grazing-incidence wide-angle X-ray scattering (GIWAXS) revealed "locked-in" morphology and superior thermal stability in **iQPH-BO** films compared to **QPMe-BO** films due to the former's H-bonding interactions. Negligible changes in UV-vis absorption were observed for **iQPH-BO** films even when annealed at temperatures over 150 °C supporting the idea that H-bonding compounds can be used to control thin-film morphology for more robust device performance.

Solid-state optical characterization of **iQPH-BO** and **QPMe-BO** revealed absorption profiles quite similar to their absorption in chloroform, which suggests that the optical properties (and aggregation state) observed in solution can be readily translated into the solid-state with only minor spectral changes. In thin films, molecular stacking was observed to be edge-on with respect to the substrate despite an intention to achieve face-on stacking. This unexpected stacking behavior highlights the complexity associated with predicting *a priori* how solution properties translate into the solid state, even with the help of computational insights and experience with related compounds. This comparative study sheds light on the advantages

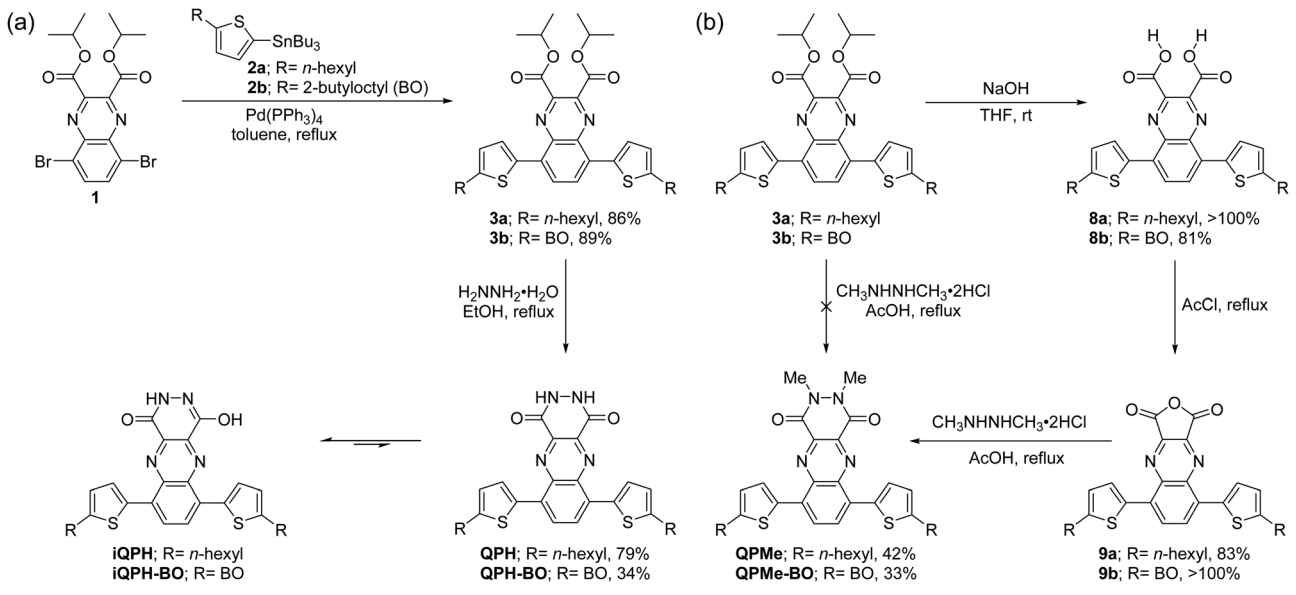

Scheme 1 Synthesis and molecular structure of (a) H-bonding capable compounds **iQPH** and **iQPH-BO** and (b) H-bonding incapable compounds **QPMe** and **QPMe-BO**.

and limitations of H-bonding mediated self-assembly towards next-generation organic optoelectronics, and the complexity associated with utilizing H-bonding to mediate the self-assembly of small molecule π-conjugated compounds.

Results and discussion

Design and synthesis

The design of the model H-bonding capable compound, **iQPH**, was inspired by the encouraging performance of previously published compounds which utilized terminal phthalhydrazide groups to facilitate self-assembly of trimeric rosettes.[36] The quinoxaline unit was inspired by synthetic compatibility and those who have applied it to great effect in organic optoelectronics;[37–39] some of the highest PCEs reported for polymeric OPVs contain quinoxaline motifs.[40–44] Quinoxaline-based compounds demonstrate good charge mobility due to their planar conjugated structure and thermal stability.[38,45] The two N atoms at the 1,4 positions make the quinoxaline moiety an electron-deficient (ED) scaffold, and it contains three pairs of substitution positions for molecular engineering.[46] Here, we fused the quinoxaline to the central phthalhydrazide to extend π-conjugation, enhance molecular planarity, and promote thermal stability. The OPV-relevant optical gap[47–49] and solubility of **iQPH** (and **iQPH-BO**) were achieved through the addition of alkyl-functionalized thiophenes to the quinoxaline-phthalhydrazide scaffold. Enhanced solubility for solution processing and solid-state characterization led to the synthesis of **iQPH-BO** and its comparator **QPMe-BO** which contain 2-butyloctyl (BO) side chains in exchange for hexyl side chains. These four compounds were successfully synthesized in multiple steps as illustrated in Scheme 1.

Through several synthetic approaches, the novel quinoxaline-based molecule **QPH**, predominantly existing in its tautomeric form **iQPH**, and its H-bonding-incapable comparator **QPMe** were successfully synthesized. The tautomeric form **iQPH** was confirmed using various characterization techniques, and our investigations revealed that the D–A systems should be built prior to condensation reactions. The intermediate diisopropyl 2,3-dioxosuccinate **1** required for the synthesis of **iQPH** was obtained following literature preparation of similar derivatives (Fig. S1, ESI‡).[50] Stille coupling in toluene was utilized to attach 2-hexylthiophene and 2-(2-butyloctyl)thiophene units to afford compounds **3a** and **3b**. Subsequent condensation with excess hydrazine monohydrate in ethanol yielded the H-bonding capable target molecules **iQPH** and **iQPH-BO** which contain the PH groups known to favor the NH/OH tautomer in certain solvents (Scheme 1a).[51,52] Confirmation of the shown tautomeric structure came through NMR characterization, DFT calculations, FT-IR experiments, and X-ray diffraction (*vide infra*).

The synthesis of the comparators **QPMe** and **QPMe-BO** was also achieved through a series of hydrolysis and condensation reactions. Starting from the hydrolysis of diester compounds **3a** and **3b** under basic conditions, diacid compounds **8a** and **8b** were afforded. The condensation reaction of compounds **8a** and **8b** generated anhydride compounds **9a** and **9b**. The last step involved a condensation reaction with 1,2-dimethylhydrazine dihydrochloride which afforded target molecules **QPMe** and **QPMe-BO** (Scheme 1b).

Establishing tautomeric structure of iQPH in solution

A thorough structural characterization of **iQPH** in solution was necessary to confirm the target molecule possessed the structure (and conformation) required for H-bonding mediated self-assembly. Interestingly, compound **iQPH** demonstrates differences in ^{1}H NMR spectral features in $CDCl_3$, DMSO-d_6, and DMF-d_7 with respect to its the thiophene protons and NH/OH protons which indicates a dynamic molecular structure. In $CDCl_3$, the proton signal at 7.8 ppm is weaker and broader compared to the analogous signals observed in DMSO-d_6 and DMF-d_7 (Fig. 2). This signal was confirmed to be an aromatic thiophene proton through H/D exchange and VT-NMR experiments (Fig. S3, ESI‡). We attribute the broadened thiophene peak of **iQPH** in $CDCl_3$ to intramolecular interactions between the thiophene proton and nitrogen atom on the quinoxaline. The C–N$\cdots$H hydrogen bonding interaction on the quinoxaline has been reported in intermolecular and intramolecular formats.[53–55] Despite DMF and DMSO often being regarded as similar polar aprotic solvents, the ^{1}H NMR spectra of **iQPH** was markedly different between these two solvents. At room temperature, two broad NH/OH peaks were observed in DMSO-d_6 around 11.64 and 12.05 ppm while a single broad peak was observed around 12.01 ppm in DMF-d_7.

VT-NMR experiments were conducted to elucidate the molecular structure of **iQPH** in DMF-d_7 and DMSO-d_6. For **iQPH** in DMSO-d_6 (Fig. 3a), two broad peaks corresponding to the NH/OH peaks are observed at room temperature. With increasing temperature, these peaks gradually shift upfield, coalesce around 55 °C, and continue to shift further upfield, indicating weakened H-bonding interactions and increased proton exchange rates. A similar trend is observed in DMF-d_7 (Fig. 3b), where the single NH/OH peak becomes shielded as the temperature increases. During the cooling process, however, this peak shifts downfield, and below −5 °C, it separates into two distinct resonances at −15 °C. These findings suggest that the proton exchange rate slows at lower temperatures which causes signal splitting. At higher temperatures, the NH/OH peaks become more shielded, coalesce into a single peak, and become broadened due to weaker H-bonding interactions and more rapid proton exchange.

Importantly, the NH and OH protons exhibit equivalent integration values across the temperature range. The integration values indicate the observed spectral changes are not due to tautomerization since this process would produce additional peaks with varying integration ratios. The data in Fig. 3 confirms **iQPH** predominantly exists in its tautomeric form in both DMF and DMSO, with solvent-specific differences in proton exchange dynamics. Although **iQPH** has an asymmetric structure, the small separation in chemical shifts at isochronous sites leads to spectral features resembling those of a symmetric structure. Overall, VT-NMR results provide robust evidence of temperature- and solvent-dependent proton exchange behavior, further supporting the dynamic nature of **iQPH** in solution.

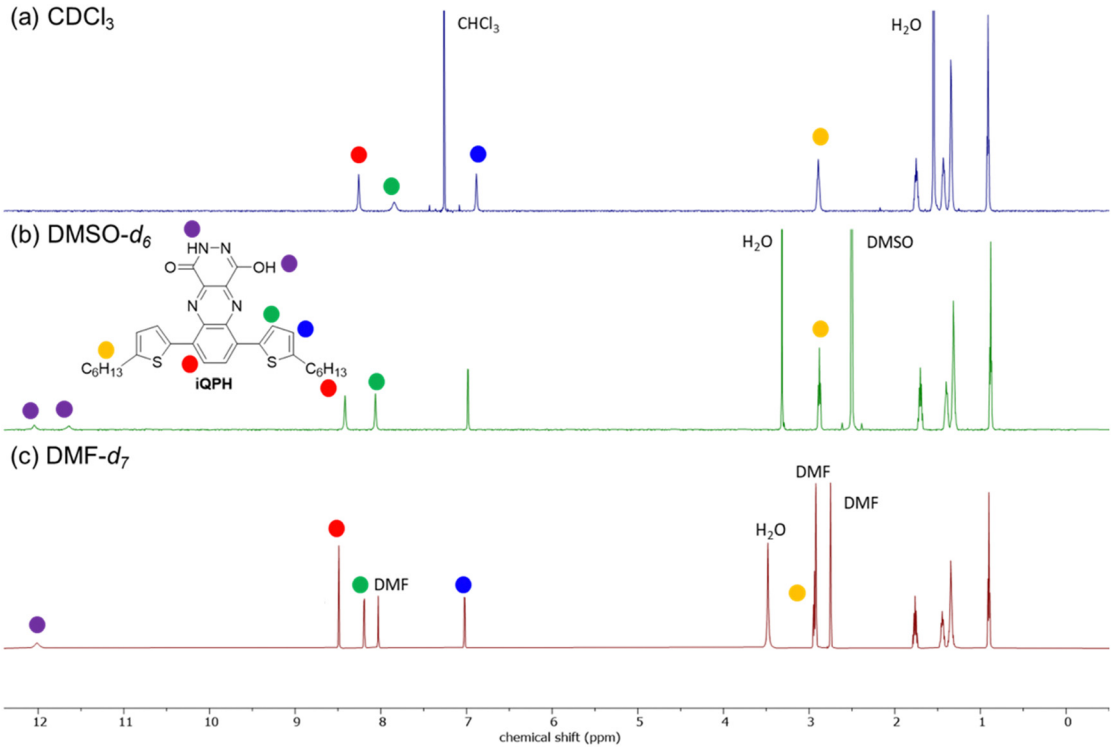

Fig. 2 ^{1}H NMR spectra of **iQPH** in (a) $CDCl_3$, (b) DMSO-d_6, and (c) DMF-d_7.

The more soluble H-bonding capable molecule, **iQPH-BO**, behaves similarly including the observed peak broadening of the thiophene proton in $CDCl_3$ (Fig. S70, ESI‡), two NH/OH peaks in DMSO-d_6 (Fig. S71, ESI‡), and a single NH/OH peak in DMF-d_7 (Fig. S72, ESI‡). For **iQPH-BO**, the weak and broad peaks from NH and OH were observed in $CDCl_3$ at room temperature unlike the **iQPH** spectra due to its superior solubility in $CDCl_3$ (Table S1, ESI‡). VT-NMR experiments reveal that **iQPH-BO** in $CDCl_3$, DMSO-d_6, and DMF-d_7 undergoes NH/OH deshielding and decoalescence at lower temperatures (Fig. S46, S52 and S53, ESI‡), consistent with increased H-bonding interactions and faster proton exchange observed for **iQPH** in DMSO-d_6 and DMF-d_7 (Fig. 3). Additionally, in $CDCl_3$, deshielding and decoalescence behaviors are observed with increasing concentration, further supporting the presence of the NH/OH tautomeric form and changes in H-bonding interactions as a function of concentration (Fig. S6, ESI‡). Taken collectively, we can conclude that **iQPH-BO** also exists in the NH/OH tautomeric form in the chosen solvents.

Single crystal X-ray diffraction

Single crystals of **iQPH** grown in warm DMF were characterized using single crystal X-ray diffraction, which further confirmed its tautomeric structure in agreement with NMR experiments and computational analysis. **iQPH** formed a solvate[56] that incorporates DMF into its monoclinic crystal system (Z = 8) (Fig. 4, Fig. S59 and S60, ESI‡). Although the DMF molecules prevented **iQPH** from forming the trimers we expected to observe, the XRD data of the **iQPH** solvate still elucidates its conformational preferences, planar structure, and π-stacking geometry.

It is evident from the XRD data that **iQPH** is highly planar with small dihedral angles between the quinoxaline and outer thiophenes units with an S22–C18–C2–C1 dihedral angle of 0.86° and C6–C5–C7–C9 dihedral angle of 3.61° (Fig. 4b). The distance H19–N29 and the distance S11–N32 are 2.35 and 2.72 Å, respectively, indicating the intramolecular interaction between the quinoxaline and thiophene spacer enhances planarity (Fig. 4b). The planarity of **iQPH** validates the molecular design in that it facilitates tight molecular packing *via* short π–π interactions. Interestingly, the preferred conformation of **iQPH** is with the thiophene spacers in two different orientations which have a slipped stacked arrangement with respect to the central quinoxaline. The π–π interaction between the thiophene spacers and quinoxaline units was calculated to be about 3.4 Å (Fig. 4c). The H-bonding geometry in **iQPH** was surprisingly complex with each **iQPH** molecule pairing with a DMF molecule and neighboring **iQPH** molecule, but in a perpendicular orientation rather than H-bonding in-plane (Fig. S59 and S60, ESI‡).

Conformational analysis of iQPH

A gas-phase conformational analysis was performed using DFT (B3LYP/6-31+G(d)) to generate low energy **iQPH** conformers as the NH/OH tautomer. Conformers were observed to have both symmetric and asymmetric thiophene units akin to what was observed in the single crystal XRD, and with O–H groups pointing towards or opposite to the N–H group. It was

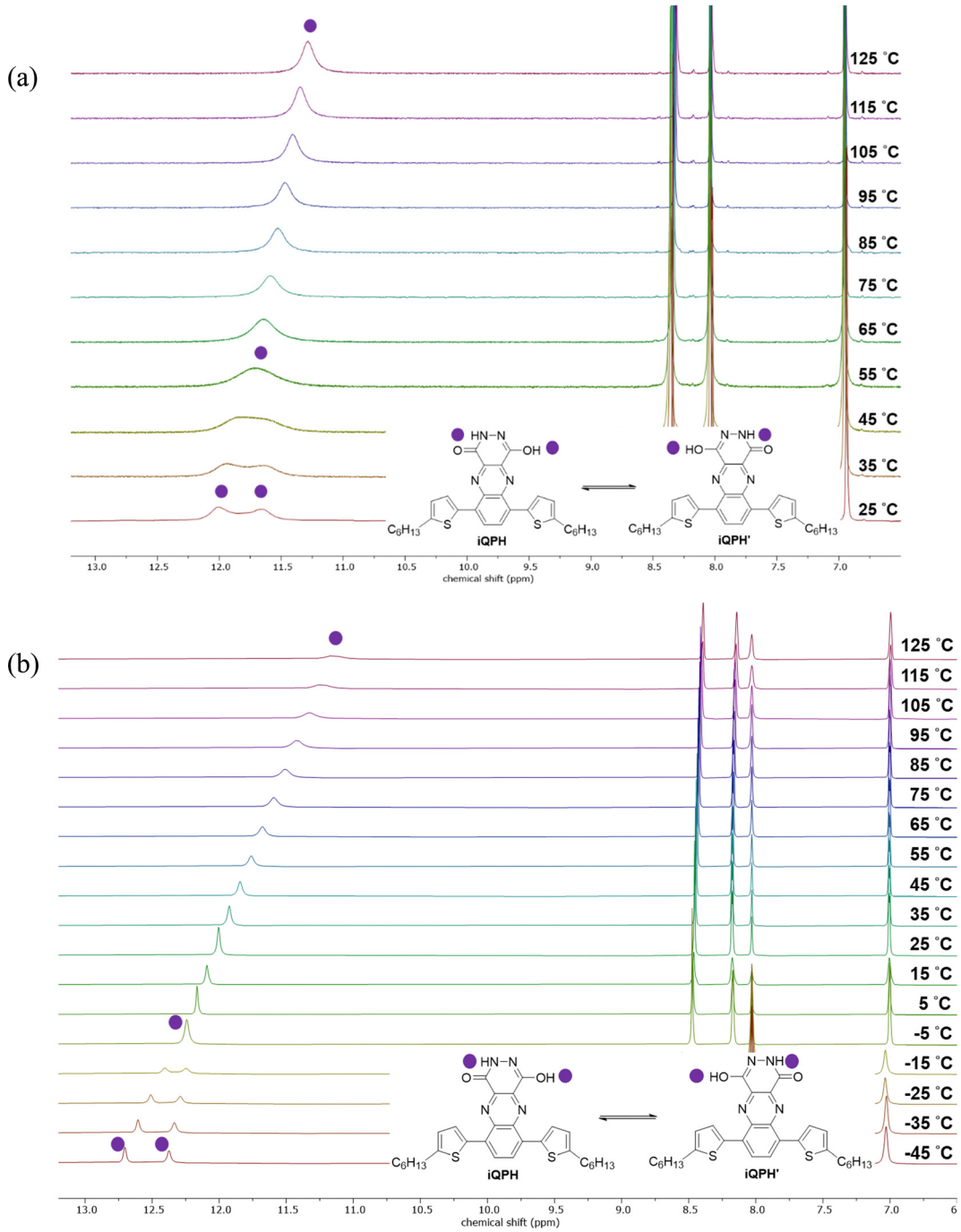

Fig. 3 (a) VT ^{1}H NMR spectra of **iQPH** in DMSO-d_6 from 25–125 °C and (b) of **iQPH** in DMF-d_7 from −45–125 °C.

determined that **iQPH_6** was the lowest energy conformer which is in a conformation with the thiophene units pointed in opposite directions and the O–H group pointed in the direction opposite of the N–H group. The conformer that represents the molecular structure observed in the XRD data is **iQPH_5** which was determined to be 1.97 kcal mol^{-1} higher in energy relative to **iQPH_6** (Fig. 5).

While the conformation of **iQPH_6** would not be suitable for trimer formation, these calculations were performed in the gas phase; hence, it may not be representative of the lowest energy conformer in solution (such as DMF). Further, it is important to note that all the conformers were within 0.5–2.5 kcal mol^{-1} of **iQPH_6**, so it is entirely plausible that several of the eight conformations for **iQPH** presented here coexist in solution and, consequently, in the solid-state, which adds even further complexity to controlling self-assembly and nanostructured morphology in thin films, especially when considering how different solvents and kinetics may influence the distribution of conformers present. Indeed, the complexity of tautomerism on supramolecular architectures has been pointed out in recent literature

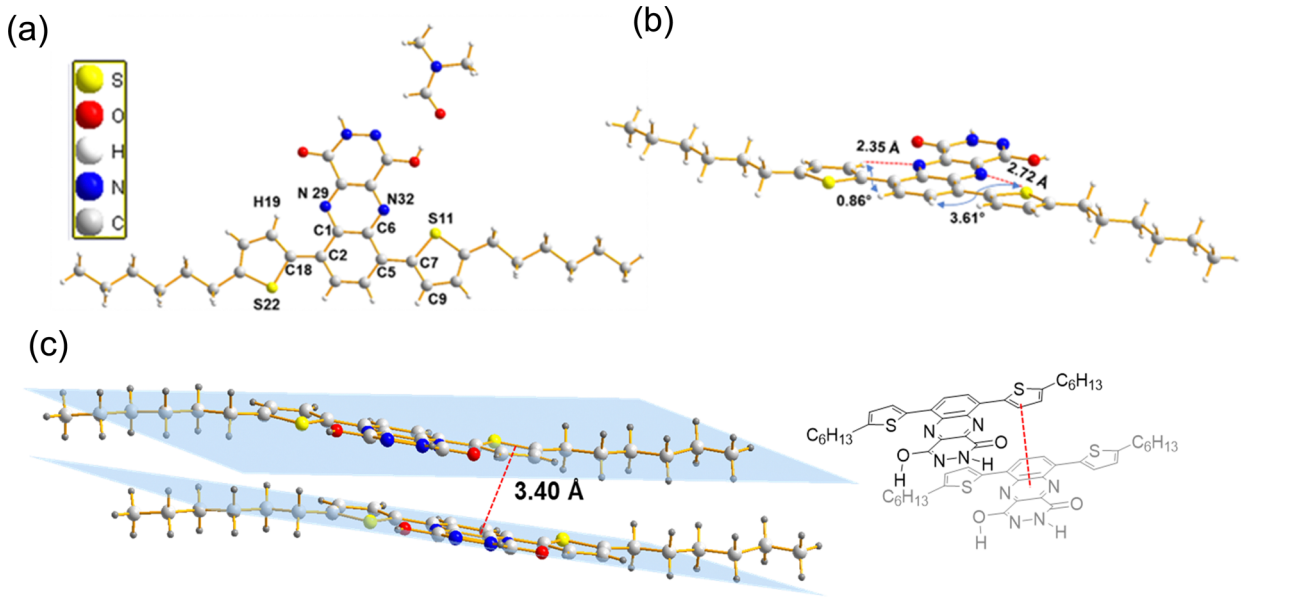

Fig. 4 Single-crystal X-ray crystallography images showing (a) ball-and-stick representation of **iQPH** H-bonded to DMF, (b) dihedral angels and distances, and (c) nearest neighbor π–π stacking distance and geometry (CCDC 2390133‡).

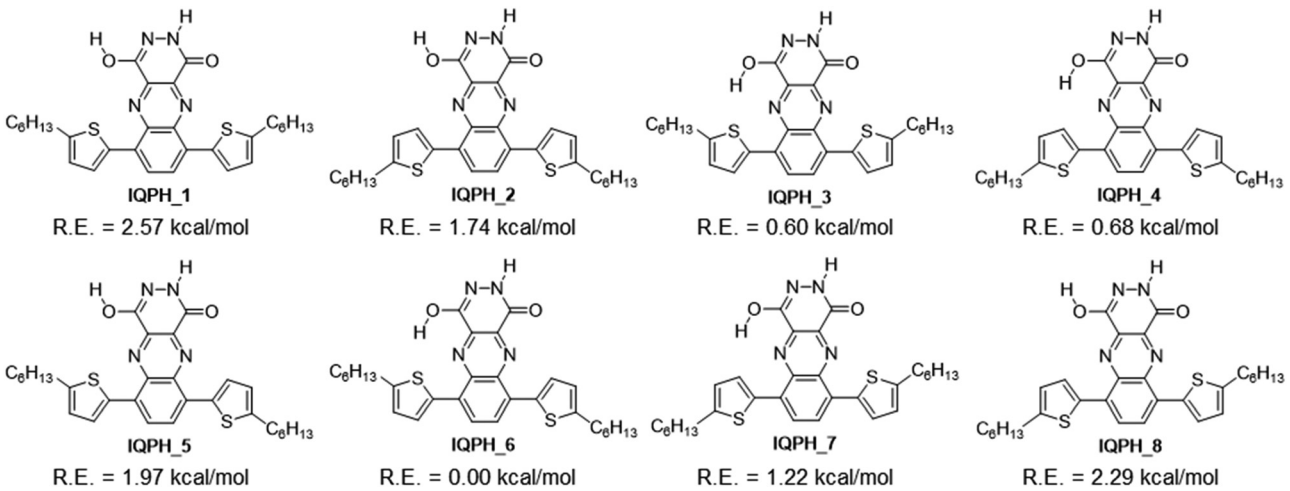

Fig. 5 Molecular structures for the eight lowest energy **iQPH** conformers in the NH/OH tautomeric form and their energies relative to **iQPH_6** (relative energy (R.E.) is the difference between the calculated most stable structure, **iQPH_6**). DFT calculation level is B3LYP/6-31+G(d) in gas phase.

and remains a key challenge to those working on self-assembled molecular structures.[57] Binding energy calculations (B3LYP/6-31+G(d), gas phase) using the conformer denoted **iQPH_2** indicated trimer formation to be thermodynamically favorable with a binding energy of 13.3 kcal mol^{-1} per molecule (Fig. S16 and Table S3, ESI‡). Therefore, under appropriate conditions, H-bonded trimers were hypothesized to be thermodynamically stable in solution and the solid state.

Diagnosing self-assembly in solution

UV-Vis spectroscopy was employed to study the self-assembling behavior of **iQPH** in solution compared to **QPMe** in different environments (solvents, concentrations, and temperatures). In all the solvents chosen for UV-vis characterization, **QPMe** and **iQPH** exhibit two major bands in their absorption profiles (Fig. 6a). The higher energy absorption band found around 300–350 nm is attributed to π–π* transitions that are localized to the thiophene units. The broader absorption band with weaker oscillator strength arises from the push–pull (D–A) characteristics of the compounds and is attributed to an intramolecular charge-transfer (ICT) transition as reported in other quinoxaline-based molecules.[50,58–61] The large separation between the π–π* and ICT transitions indicates strong ICT characteristics within the D–A chromophores (Fig. 6b and c).[62–64] Because the ICT peak is positioned more optimally for visible (solar) light absorption and is more sensitive to solvent polarity (sensing), we focused the spectral analysis on this optical transition ($\lambda_{max,vis}$). The solution absorption profiles of

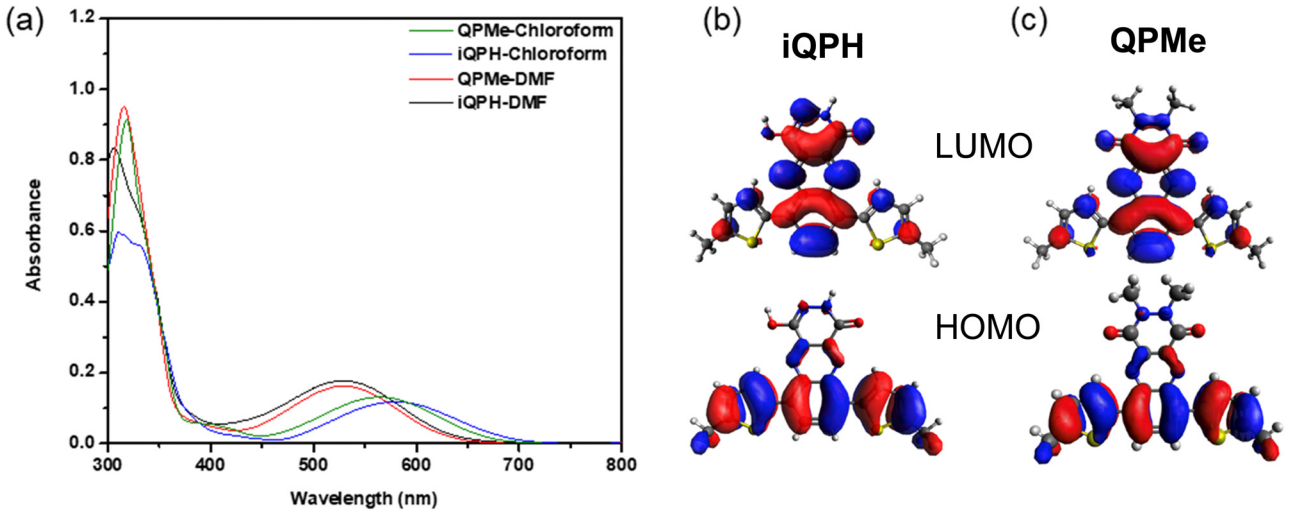

Fig. 6 (a) Absorption spectra of 20 μM **QPMe** and **iQPH** in chloroform and DMF and (b) and (c) Frontier molecular orbital diagrams of **iQPH** and **QPMe**.

QPMe and **iQPH** obtained in various solvents demonstrate significant negative solvatochromism with $\lambda_{max,vis}$ spanning 46 nm for **iQPH** and 37 nm for **QPMe** (Fig. S22, ESI‡). Both **QPMe** and **iQPH** have $\lambda_{max,vis}$ around 530 nm in polar solvents (DMF, DMSO, and acetone), while they display the most redshifted absorption in nonpolar and halogenated solvents, especially in chloroform (Fig. 6a). The redshifted absorption of **QPMe** and **iQPH** in chloroform is suspected to arise from significant aggregation through π–π interactions and the ICT ground state being less stabilized compared to the polar solvents. The optical absorption data of **QPMe** and **iQPH** in different solvents are summarized in Table S5 (ESI‡).

In most of the selected solvents, the H-bonding capable compound **iQPH** exhibits more redshifted absorption than the H-bonding incapable compound **QPMe** in agreement with TD-DFT calculations (Tables S4 and S5, ESI‡). We suspect the additional redshift in absorption of **iQPH** relative to **QPMe** is from its stronger ICT character and enhanced planarity from intermolecular H-bonding and supramolecular assembly. Further evidence for H-bonding interactions in solution comes from UV-vis of **iQPH** and **iQPH-BO** in chloroform with small additions of a hydrogen bonding capable solvent like ethanol or methanol. Upon adding a few percentages of these solvents, the absorption spectra of **iQPH-BO** and **iQPH** blueshift by 12 nm and 24 nm, respectively, due to the disruption of intermolecular H-bonding which facilitates greater electron delocalization between nearest neighbor molecules (Fig. S61, ESI‡). Because the absorbance spectra only show minor blueshifts upon adding additional ethanol or methanol beyond 2–10% (by volume), we do not propose that solvatochromism explains the blueshifted absorbance. The larger blueshift observed for **iQPH** is attributed to its stronger H-bonding interactions due to its shorter alkyl chains compared to **iQPH-BO**. While **QPMe** and **iQPH** both show negative solvatochromic behavior, their shifts in absorption do not neatly obey trends in solvent polarity because planar solvents like toluene can disrupt π-stacking,[63] and the disaggregation of **iQPH** is greater than **QPMe** in solvents that can participate in hydrogen bonding (DMF, DMSO).

Concentration-dependent UV-vis spectroscopy

Beer–Lambert plots were produced for **iQPH** and **QPMe** in chloroform and DMSO which showed no nonlinearity or spectral shifts over the selected concentration ranges (Fig. S23–S26, ESI‡). However, in DMF, it was evident that the $\lambda_{max,vis}$ of **iQPH** redshifted 6 nm with increasing concentrations (Fig. S28, ESI‡) while **QPMe** again showed no concentration dependent behavior (Fig. S27, ESI‡). At higher concentrations, the **iQPH** self-aggregation begins to dominate over the interactions with H-bonding capable DMF molecules which is an important consideration when trying to control supramolecular assembly in solution with the desire of translating the molecular assemblies to the solid state. Since higher concentrations than those studied in this concentration-dependent study would be utilized during the fabrication of thin films, the extent to which DMF disrupts H-bonding is likely to decrease but still remain. Therefore, when solution processing films with the H-bonding capable materials, we opted to utilize chloroform to allow self-assembly and trimer formation.

Temperature-dependent UV-vis spectroscopy

Variable-temperature UV-vis (VT-UV-vis) experiments were used to assess the temperature dependent aggregation and self-assembling behavior of **iQPH** and **QPMe** in different solvents. The absorbance spectra recorded during heating are noted as °C1, while those recorded during cooling are noted °C2. In chloroform and DMSO, a 3–7 nm blueshift was observed for **iQPH** and **QPMe** during heating from room temperature (25 °C1) to the highest operating temperature (55 °C1 for chloroform samples and 95 °C1 for DMSO samples) accompanied by a decrease in absorbance (Fig. S29a–S32a, ESI‡). These spectral changes are attributed to disaggregation through the disruption of π–π interactions. Once the highest operating temperature was reached, the temperature was held, and

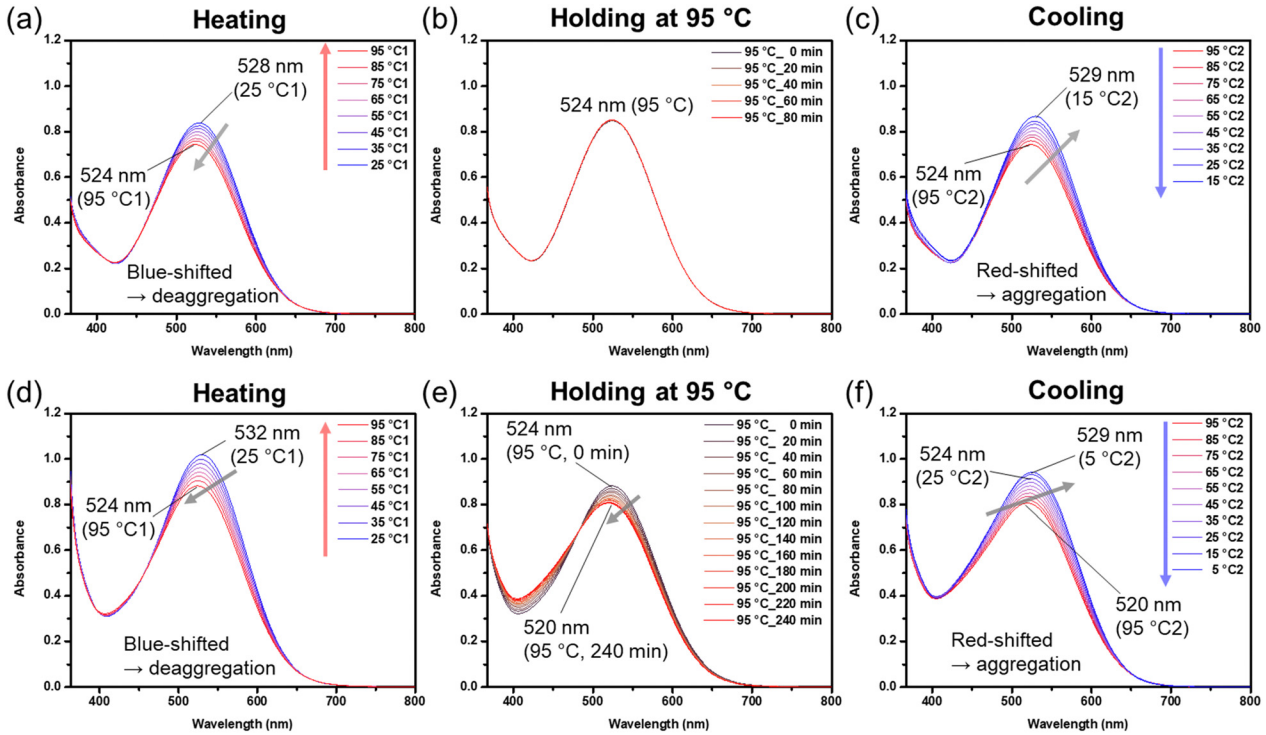

Fig. 7 Variable-temperature UV-vis of 120 μM **QPMe** in DMF (a) during heating, (b) holding temperature at 95 °C, and (c) during cooling, and 120 μM **iQPH** in DMF (d) during heating, (e) holding temperature at 95 °C, and (f) during cooling.

absorbance measurements were taken every 20 minutes over an 80-minute time frame which showed no obvious spectral changes (Fig. S29b–S32b, ESI‡).

Once the solutions were cooled to their original temperature, the original absorption profiles were obtained. In DMF, **QPMe** again exhibits a blueshift during heating, a redshift during cooling, and no shift in $\lambda_{max,vis}$ while holding the temperature constant at 95 °C (Fig. 7a–c). In contrast, **iQPH** continues to undergo additional disaggregation when the temperature is held at 95 °C (Fig. 7e) evidenced by continual blueshifting which is a unique observation and was not observed for **iQPH** in the other chosen solvents. While heating **iQPH** in DMF at 95 °C, the $\lambda_{max,vis}$ continues to blueshift by 4 nm over 4 hours in addition to peak broadening (Fig. 7e). After cooling the solution back to room temperature, the absorbance spectra remain broadened and blueshifted, which indicates a new aggregation state was achieved in DMF (Fig. S35, ESI‡). The isosbestic point around 485 nm during the constant heating phase also suggests the coexistence of two or more kinds of absorbing species in equilibrium.

We suspect that these observations correspond to the dissociation of **iQPH** H-bonded aggregates (*e.g.*, trimers) by DMF at elevated temperatures, which is supported by the X-ray diffraction studies of single crystals of **iQPH** grown in warm DMF (see above). After dissociating **iQPH**, the DMF solvent molecules solvate the dissociated monomers to form **iQPH**-DMF dimers and possibly other types of aggregates which are preserved after cooling the sample back to room temperature. **iQPH-BO** displayed similar temperature-dependent behavior in the same solvents (Fig. S34 and S36, ESI‡). The changes to intermolecular interactions observed in these temperature-dependent studies highlight how the kinetics of self-assembly processes may occur over minutes, hours, or longer and are important to consider before processing H-bonding materials into films for optoelectronic devices.[65] Additional VT-UV-vis experiments for **iQPH** in DMF were carried out with prolonged heating at lower temperatures (55–85 °C), which showed that the ability of DMF to disrupt the self-aggregation of **iQPH** was minimal below 75 °C (Fig. S39–S42, ESI‡). The unique thermal history **iQPH** exhibited in DMF was not observed in any of the **QPMe** solutions and suggests that **iQPH** is able to self-assemble at concentrations as low as 20 μM, which exemplifies its strongly aggregating nature (Fig. S37 and S38, ESI‡). These VT-UV-vis experiments also support that **iQPH** likely exists as stable π-stacked, H-bonded aggregates in chloroform where no disruption of intermolecular H-bonding would be present. Although the π–π interactions between aggregates are likely to be disrupted at higher temperatures, the H-bonds in trimers or other aggregates are predicted to remain intact when heated to mild temperatures.

^{1}H NMR spectroscopy was also utilized to provide additional insight into the assembly and aggregation of **iQPH** and **QPMe** (and their more soluble versions) in different environments as 450 μM solutions. Changes in chemical shift for the aromatic and aliphatic peaks were observed for all four of the synthesized compounds in $CDCl_3$, DMF-d_7, and DMSO-d_6 as the temperature was increased or decreased corresponding to changes in intermolecular interactions (Fig. S45–S54, ESI‡).

As the temperature of the solutions was decreased from the starting to temperature (55 °C for $CDCl_3$ and 125 °C for DMF-d_7/DMSO-d_6), the aromatic protons tended to become more deshielded indicating an increase in π–π interactions (Tables S6 and S7, ESI‡). Unlike the aromatic protons, the aliphatic protons tended to become more shielded as the temperatures decreased, possibly due to weaker van der Waals interactions between the solubilizing chains (Tables S6 and S7, ESI‡). The interplay of H-bonding, π–π, and van der Waals interactions ultimately drive how these molecules assemble (or disassemble), so comparing how the different alkyl chain length affects aggregation in the hexyl and butyloctyl versions of the compounds is important from a molecular design stand point as has been pointed out recently.[66] We did not observe that the change in chemical shift for the aliphatic protons was noticeably different between the model compounds and their BO-versions, suggesting that the dissimilar alkyl chains did not dramatically change aggregation behavior (Tables S6 and S7, ESI‡). In general, the **iQPH-BO** and **QPMe-BO** samples demonstrated similar changes in the chemical shifts for their aromatic and aliphatic protons compared to their less soluble versions.

Wavelength-dependent photoluminescence

The equilibrium of **iQPH** and **QPMe** monomers and aggregates in solution was also studied using photoluminescence (PL) spectroscopy. In chloroform and DMF, the PL spectra of **QPMe** and **iQPH** were observed to be strongly dependent on the excitation wavelength due to emission occurring through the π–π* and/or ICT transitions, with the latter occurring at longer wavelengths (Fig. 8, Fig. S62 and S63, ESI‡). The PL intensity from each transition also depends on the extent of aggregation from π–π and H-bonding interactions which can promote nonradiative relaxation mechanisms, especially for the π–π* transition.

It has been previously reported how ICT transitions are often weakly emissive with large Stokes shifts,[67,68] which we observe here as well (Fig. S63, ESI‡). The large Stokes shift and weak emission can be explained by the significant structural reorganization of the ICT state upon excitation. Gaussian peak fitting of the absorbance spectra for **iQPH** and **QPMe** reveals the different excitonic and vibronic states that are predicted to facilitate these distinctive emission pathways (Fig. 8). While it is challenging to state the physical origins of the deconvoluted peaks concretely, the three lower energy peaks are assigned to the ICT manifold, while the three higher energy peaks are associated with the π–π* manifold localized along the thiophenes.

In chloroform, the PL intensity is much weaker compared to DMF for both compounds (and their more soluble versions) suggesting that the molecules are more aggregated in chloroform and are more prone to internal conversion and partially due to the inner filter effect (Fig. S63, ESI‡).[69] For both **QPMe** and **iQPH**, the spectral range of PL emission is much greater in DMF compared to chloroform because the π–π* transition is more favored in DMF, while the ICT transition is less stabilized and is less emissive than in chloroform (Fig. 8 and Fig. S63, ESI‡). The excitation-wavelength-dependent photoluminescence highlights the environmental sensitivity of the ICT transition which is interesting in terms of chemical sensing, and the strong ICT character of these compounds is favorable in OPV contexts where charge separation is crucial.[70–72]

Solid-state optical properties

Thin-film absorption and PL spectra were obtained for **iQPH-BO** and **QPMe-BO** to understand how the presence or lack of H-bonding interactions influences solid-state packing and optoelectronic properties (Fig. 9). Interestingly, the thin film absorption is blueshifted relative to its solution absorption in chloroform by 22 nm for **iQPH-BO** and 2 nm for **QPMe-BO**. This again demonstrates how chloroform induces a negative solvatochromic effect in solution, particularly on the ICT transition (more so for **iQPH-BO** since it is more polar), and that this effect is not compensated by tighter intermolecular interactions in the solid-state which usually redshifts absorption due to greater electron delocalization. The fact that the solution and thin film absorption have such similar profiles suggests these molecules are strongly aggregated in solution, which is understandable given their planar structure and conjugation, and that the films are amorphous or have primarily short-range order.

The absorption spectrum for as-spun **iQPH-BO** films was 39 nm redshifted compared to that of as-spun **QPMe-BO** films. After annealing at 90 °C for 30 minutes, the **QPMe-BO** films undergo a 33 nm red shift in absorbance and a 10 nm redshift in PL, while the absorbance and PL for annealed **iQPH-BO** films remains essentially unchanged (Fig. 9). From this data, it is evident that the **iQPH-BO** morphology is considerably more stable or locked in compared to **QPMe-BO**, which we again attribute to intermolecular H-bonding interactions and supramolecular assemblies. With the $\lambda_{max,vis}$ of annealed **iQPH-BO** and **QPMe-BO** films at 562 nm and 553 nm, respectively, only a 10 nm difference in max absorption is observed like what was observed in solution. While both the as-spun **iQPH-BO** and **QPMe-BO** films display a single broad $\lambda_{max,vis}$, the annealed **QPMe-BO** film displays a vibronic shoulder around 590 nm, which indicates enhanced crystallinity. In thin films, neither material displays emission from the π–π* transition and exhibited only faint emission from the ICT state, which is favorable for photovoltaic applications. The optical properties of **iQPH-BO** and **QPMe-BO** from thin film measurements and electrochemical characterization are summarized in Table S9 (ESI‡).

Thermal stability of iQPH-BO and QPMe-BO

To assess the structural stability of **iQPH-BO** and **QPMe-BO** in thin films, thermal annealing was performed up to 200 °C (Fig. 10). The **QPMe-BO** film was observed to undergo a morphological change to a metastable phase at a much lower temperature (around 90 °C), whereas **iQPH-BO** appeared to be stable up to ~175 °C, which again highlights how H-bonding can facilitate thin film thermal stability and consistent film morphology. Around 110 °C, **QPMe-BO** begins to melt and bead up on glass substrates, which ruins its metastable crystal

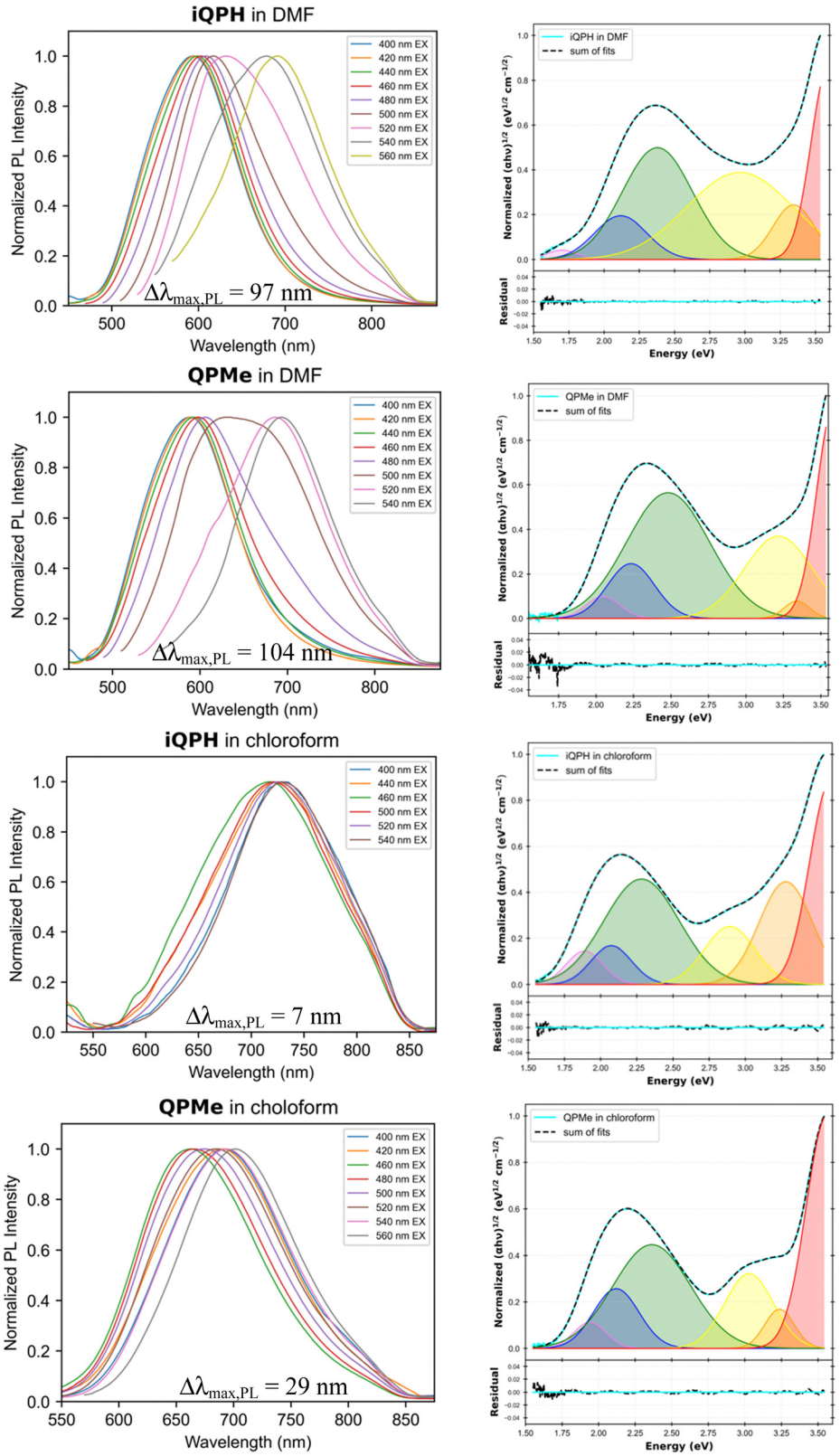

Fig. 8 Normalized PL intensity of **iQPH** and **QPMe** in chloroform and DMF at 100 μM at various excitation wavelengths (left). Gaussian fits to the absorbance spectra of **iQPH** and **QPMe** in chloroform and DMF (right).

structure and results in an increase in diffuse reflectance (Fig. 10b). This same phenomenon was observed with **iQPH-BO** films, but the onset of these morphological changes was not observed at significantly higher temperatures, around 175 °C (Fig. 10a).

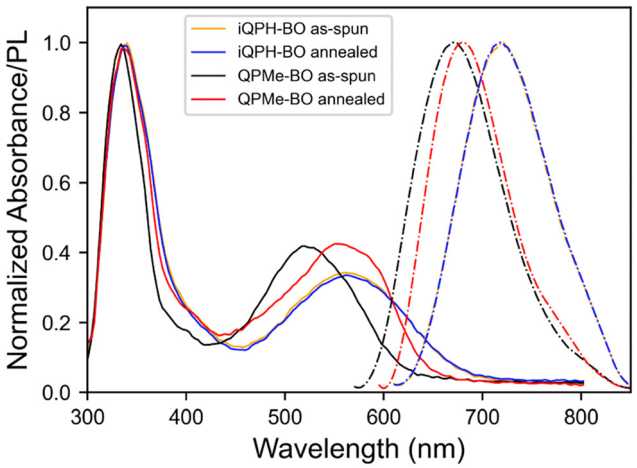

Fig. 9 Normalized UV-vis absorption (solid lines) and normalized photoluminescence (PL, dashed lines) spectra for as-spun and thermally annealed films of compounds **iQPH-BO** and **QPMe-BO**. An excitation wavelength of 540 nm was used to obtain the PL spectra.

The resistance to structural changes in the solid-state is suspected to be due to π-stacked **iQPH-BO** H-bonded aggregates (plausibly trimers), which are unlikely to experience significant diffusion due to their bulky nature. Thermal stability was also assessed using thermogravimetric analysis (TGA) which showed the decomposition temperature for **iQPH** (371 °C) is about 15 °C higher than **QPMe** (356 °C), providing indirect evidence for H-bonded aggregation (Fig. S56a, ESI‡). The –BO versions, **iQPH-BO** and **QPMe-BO**, also demonstrated similar thermal decomposition profiles as **iQPH** and **QPMe**, but with smaller differences in decomposition temperatures: 367 °C for **iQPH-BO** and 366 °C for **QPMe-BO** (Fig. S56b, ESI‡).

Differential scanning calorimetry (DSC) data was also obtained, which showed **QPMe** undergoes obvious melting and recrystallization processes, although hysteresis was observed over heating and cooling cycles (Fig. S57b, ESI‡). In contrast, **iQPH** was observed to melt during the first heating cycle, but no subsequent melting or crystallization events were observed (Fig. S57a, ESI‡). This data suggests that the rate of nucleation is quite fast, and longer time periods (slower cooling) may be required to achieve crystallization. This rapid nucleation and lack of crystallization could be explained by the conformer distribution of the **iQPH** molecules as described in the DFT conformer search data, or due to the strength of the H-bonding interactions prohibiting the diffusion required to form crystallites. This short-range order of **iQPH-BO** was also observed in AFM topographical images (see below) and is consistent with the thin film absorbance data. During the heating phases of the second and third cycles, **iQPH** may undergo a subtle glass transition rather than a true melting event. Either way, this interesting behavior again highlights how **iQPH** experiences less structural change over a wider temperature range compared to **QPMe**.

Atomic force microscopy

The changes in thin-film morphology during thermal annealing were also studied using AFM, which correlate well to the observed optoelectronic properties (Fig. 11). The height images of the as-spun films for **QPMe-BO** and **iQPH-BO** indicate low roughness and amorphous morphologies. After annealing at 90 °C, the **QPMe-BO** film exhibited drastically increased root-mean-square roughness (R_{RMS}), from 1 nm to 18 nm, and significantly larger grains, indicative of increased crystallinity (Fig. 11c and d). When the **iQPH-BO** film was annealed at 110 °C, only minor structural changes over very short distances were observed (Fig. 11a and b).

Under close inspection, the annealed **iQPH-BO** film was observed to form small crystallites roughly 1 nm in height and 10 nm in length. The fine-grained nanostructure of annealed **iQPH-BO** films seems to indicate diffusion-limited recrystallization which was recently shown to bestow superior thermal stability in non-fullerene based solar cells.[72] Annealed

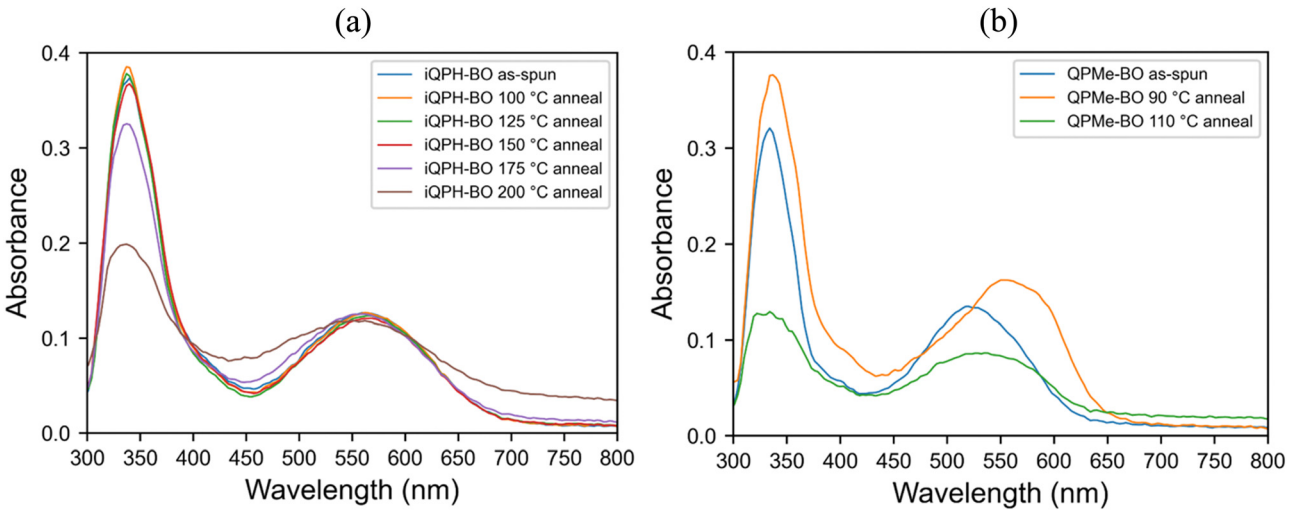

Fig. 10 UV-Vis absorption spectra for (a) **iQPH-BO** and (b) **QPMe-BO** over increasing annealing temperatures. Films were annealed for 15 minutes at each temperature.

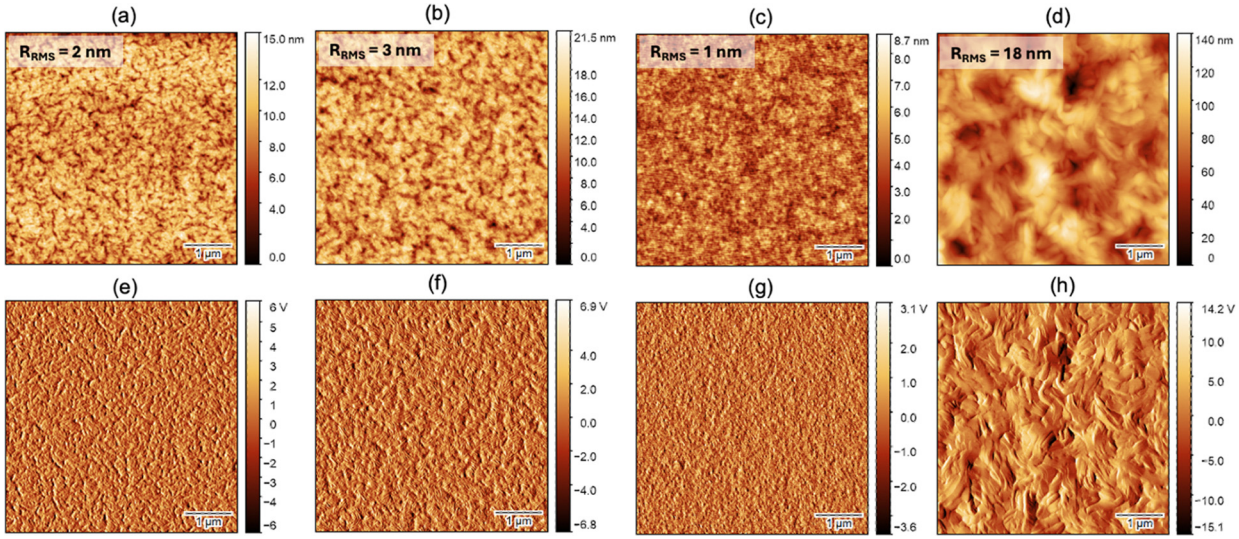

Fig. 11 AFM height images of (a) **iQPH-BO** films that are as-spun and (b) thermally annealed and of **QPMe-BO** films that are (c) as-spun and (d) thermally annealed. Below each height image is the corresponding amplitude error image (e)–(h) to display the surface pseudo-topography.

QPMe-BO films, in contrast, show the ability to undergo long-range diffusion crystallization, which would bear out poorly in a bulk heterojunction environment where stable morphologies are desired. The different morphological stability between the two model compounds highlights the tradeoff that exists between enhanced crystallinity after thermal annealing, which is likely to enhance charge transport of donor or acceptor domains (in the case of **QPMe-BO**), and stable morphology which is essential for exciton separation and charge transport (like **iQPH-BO**).

Thin-film X-ray diffraction

To probe the molecular orientation in thin films, we employed GIWAXS measurements on neat films of **iQPH-BO** and **QPMe-BO** on glass substrates (Fig. 12). Both compounds exhibited five main diffraction peaks with the parameters summarized in Table S11 (ESI‡). It is again evident from the GIWAXS data that the thin-film morphology changes minimally for **iQPH-BO** films after annealing at 110 °C, but the crystallinity increases for **QPMe-BO** after annealing at 90 °C. For **QPMe-BO**, the diffraction peaks around 2θ = 3.6° and 22° grow in intensity with the peak width becoming narrower, consistent with an increase in crystallinity.

The *d*-spacings associated with the peaks at ~22.5° are consistent with π–π stacking distances, which are 0.1 nm shorter for **iQPH-BO** (3.9 nm) compared to **QPMe-BO** (4.0 nm), presumably from enhanced planarity from H-bonding interactions (Table S11, ESI‡). Despite the previously reported H-bonding compounds stacking vertically relative their substrate,[4,35] **iQPH-BO** and **QPMe-BO** were found to preferentially stack edge-on with respect to the substrate evidenced by the diffraction peak around 2.1° (*d*-spacing ~4.2 nm) being hundreds of times more intense than the other peaks. While not optimal for OPVs, this edge-on stacking arrangement may facilitate efficient charge transport parallel to the substrate in devices like thin-film transistors. Taken collectively, the solid-state characterization of **QPMe-BO** and **iQPH-BO** demonstrates clearly that the H-bonding interactions and putative trimer formation inherent to **iQPH-BO** allow it to achieve morphologically stable films over much wider temperature ranges with optical properties that remain similarly consistent.

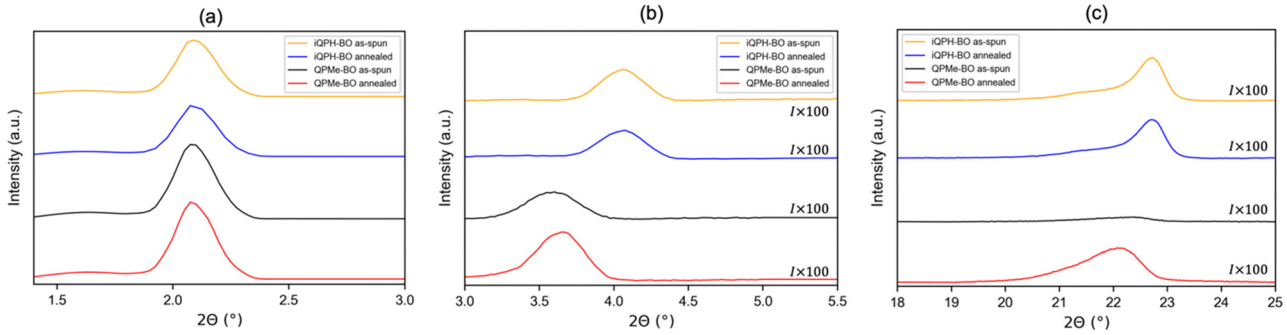

Fig. 12 Grazing-incidence wide-angle X-ray scattering (GIWAXS) $\theta - 2\theta$ diffraction patterns for as-spun and thermally annealed films of **iQPH-BO** and **QPMe-BO**. The plots (a–c) were separated along 2θ and the intensities in (b) and (c) were scaled up by 100 for clarity.

Numerous attempts at making various devices including BHJ OPVs, hole-only-devices, and thin-film transistors (TFTs) with the model compounds yielded inconsistent performance, making it hard to draw meaningful conclusions from the data and comparisons between the H-bonding capable and incapable materials. In short, phase separation between the model compounds and fullerene-based acceptors severely limited OPV performance. For TFTs and HODs, thin film uniformity following spin coating led to inconsistent current–voltage behavior. The strongly aggregating nature of these materials proved very challenging for device fabrication which necessitates further work to improve molecular design, substrate preparation through interfacial engineering, and other optimizations that were unable to be achieved so far.

Conclusion

To conclude, we have presented a novel design strategy involving an electron donating phthalhydrazide moiety and quinoxaline to create donor–acceptor molecules with self-assembling abilities for optoelectronic applications. The compound **iQPH** and its comparator **QPMe** were successfully synthesized in addition to their more soluble versions **iQPH-BO** and **QPMe-BO**. Through NMR techniques, DFT calculations, and single crystal XRD, the tautomeric form of **iQPH** and **iQPH-BO** were confirmed which is essential to achieve the desired supramolecular self-assembly. UV-Vis spectroscopy, ^{1}H NMR, and photoluminescence spectroscopy were utilized to evaluate how these compounds' optoelectronic properties and molecular organization interactions change in various environments. The H-bonding mediated self-assembly of **iQPH** and **iQPH-BO** were detected through VT-UV-vis experiments where DMF was observed to dissociate H-bonded molecular assemblies. Solution studies revealed significant solvatochromism of the ICT transition highlighting the strong push–pull electronics of the designed molecules and potential for sensing applications. Solid-state characterization of **QPMe-BO** thin films showed significant changes in film absorption and morphology after annealing around 90 °C, while structural and morphological changes in **iQPH-BO** films were not observed until much higher temperatures. These results provide evidence that H-bonding interactions can lock in the morphology in the film which is attractive for OPVs employing the BHJ architecture. While this locked in morphology indicates progress towards achieving programmable solid-state structures, the **iQPH-BO** films only displayed short range order, even after thermal annealing, and displayed unexpected edge-on stacking which is not ideal for charge transport in the photoactive layers of OPVs. With further improvement to molecular design, we hope to further enhance solubility for better blending with popular electron accepting materials, substrate wetting, and molecular stacking that is face on relative to the substrate to facilitate efficient charge transport.

Author contributions

The manuscript was written through contributions of all authors. All authors have given approval to the final version of the manuscript.

Data availability

The data supporting this article have been included as part of the ESI.‡ Crystallographic data for **iQPH** has been deposited at the CCDC under 2390133.

Conflicts of interest

There are no conflicts of interest to declare.

Acknowledgements

R. K. C. and J. X. are thankful to the National Science Foundation for supporting this research (CHE-1904534 and CHE-2203754). K. A. A. is grateful to the National Science Foundation for funding the X-ray diffractometer (CHE-1828064). The mass spectrometric data were obtained by the UF Department of Chemistry Mass Spectrometry Research and Education Center supported, in part, by the National Institutes of Health (NIH S10OD021758-01A1). Acknowledgment is made to National Science Foundation for funding support of this research (CHE-1904534 and CHE-2203754). K. A. A. is grateful to the National Science Foundation for funding the X-ray diffractometer (CHE-1828064). We acknowledge the University of Florida Research Computing for providing computational resources and support that have contributed to the research results reported in this publication (**https://www.rc.ufl.edu**). We would also like to thank the UF Center for Nuclear Magnetic Resonance Spectroscopy for providing equipment and support that have contributed to these published results.

References

1 Z. B. Henson, K. Müllen and G. C. Bazan, *Nat. Chem.*, 2012, **4**, 699–704.
2 H. Bronstein, C. B. Nielsen, B. C. Schroeder and I. McCulloch, *Nat. Rev. Chem.*, 2020, **4**, 66–77.
3 S. I. Stupp and L. C. Palmer, *Chem. Mater.*, 2014, **26**, 507–518.
4 A. O. Weldeab, C. T. Kornman, L. Li, D. J. Starkenburg, X. Zhao, D. E. Fagnani, S. J. Sadovy, S. S. Perry, J. Xue and R. K. Castellano, *Org. Mater.*, 2021, **03**, 390–404.
5 J. A. Elemans, A. E. Rowan and R. J. Nolte, *J. Mater. Chem.*, 2003, **13**, 2661–2670.
6 L. Lu, T. Zheng, Q. Wu, A. M. Schneider, D. Zhao and L. Yu, *Chem. Rev.*, 2015, **115**, 12666–12731.
7 Q. An, F. Zhang, J. Zhang, W. Tang, Z. Deng and B. Hu, *Energy Environ. Sci.*, 2016, **9**, 281–322.
8 A. Zumeit, A. S. Dahiya, A. Christou, D. Shakthivel and R. Dahiya, *npj Flexible Electron.*, 2021, **5**, 18.

9 Y. Lin, Y. Li and X. Zhan, *Chem. Soc. Rev.*, 2012, **41**, 4245–4272.
10 A. Mishra and P. Bäuerle, *Angew. Chem., Int. Ed.*, 2012, **51**, 2020–2067.
11 W. Li, X. Zhang, X. Zhang, J. Yao and C. Zhan, *ACS Appl. Mater. Interfaces*, 2017, **9**, 1446–1452.
12 H. Zhou, Y. Zhang, J. Seifter, S. D. Collins, C. Luo, G. C. Bazan, T.-Q. Nguyen and A. J. Heeger, *Adv. Mater.*, 2013, **25**, 1646–1652.
13 D. H. Wang, J. S. Moon, J. Seifter, J. Jo, J. H. Park, O. O. Park and A. J. Heeger, *Nano Lett.*, 2011, **11**, 3163–3168.
14 J. S. Moon, C. J. Takacs, Y. Sun and A. J. Heeger, *Nano Lett.*, 2011, **11**, 1036–1039.
15 C. J. Takacs, N. D. Treat, S. Krämer, Z. Chen, A. Facchetti, M. L. Chabinyc and A. J. Heeger, *Nano Lett.*, 2013, **13**, 2522–2527.
16 E. Verploegen, R. Mondal, C. J. Bettinger, S. Sok, M. F. Toney and Z. Bao, *Adv. Funct. Mater.*, 2010, **20**, 3519–3529.
17 J. K. Lee, W. L. Ma, C. J. Brabec, J. Yuen, J. S. Moon, J. Y. Kim, K. Lee, G. C. Bazan and A. J. Heeger, *J. Am. Chem. Soc.*, 2008, **130**, 3619–3623.
18 J. S. Moon, C. J. Takacs, S. Cho, R. C. Coffin, H. Kim, G. C. Bazan and A. J. Heeger, *Nano Lett.*, 2010, **10**, 4005–4008.
19 O. D. Lourenco, L. Benatto, C. F. N. Marchiori, H. C. Avila, N. A. D. Yamamoto, C. K. Oliveira, M. G. E. da Luz, M. Cremona, M. Koehler and L. S. Roman, *J. Phys. Chem. C*, 2017, **121**, 16035–16044.
20 Y.-J. Cheng, S.-H. Yang and C.-S. Hsu, *Chem. Rev.*, 2009, **109**, 5868–5923.
21 M. T. Dang, L. Hirsch, G. Wantz and J. D. Wuest, *Chem. Rev.*, 2013, **113**, 3734–3765.
22 S. Scholz, D. Kondakov, B. Lüssem and K. Leo, *Chem. Rev.*, 2015, **115**, 8449–8503.
23 L. Dou, Y. Liu, Z. Hong, G. Li and Y. Yang, *Chem. Rev.*, 2015, **115**, 12633–12665.
24 S. Park, T. Kim, S. Yoon, C. W. Koh, H. Y. Woo and H. J. Son, *Adv. Mater.*, 2020, **32**, 2002217.
25 W. R. Mateker and M. D. McGehee, *Adv. Mater.*, 2017, **29**, 1603940.
26 N. Grossiord, J. M. Kroon, R. Andriessen and P. W. M. Blom, *Org. Electron.*, 2012, **13**, 432–456.
27 S. Yagai, M. Suzuki, X. Lin, M. Gushiken, T. Noguchi, T. Karatsu, A. Kitamura, A. Saeki, S. Seki, Y. Kikkawa, Y. Tani and K. Nakayama, *Chem. – Eur. J.*, 2014, **20**, 16128–16137.
28 A. Mourran, U. Ziener, M. Möller, M. Suarez and J.-M. Lehn, *Langmuir*, 2006, **22**, 7579–7586.
29 T. Kaseyama, S. Furumi, X. Zhang, K. Tanaka and M. Takeuchi, *Angew. Chem., Int. Ed.*, 2011, **50**, 3684–3687.
30 M. Suárez, J.-M. Lehn, S. C. Zimmerman, A. Skoulios and B. Heinrich, *J. Am. Chem. Soc.*, 1998, **120**, 9526–9532.
31 J. Otsuki, Y. Okabe, S. Eitaki, Y. Sei and K. Yamaguchi, *Chem. Lett.*, 2006, **35**, 1256–1257.
32 B. M. Schulze, N. T. Shewmon, J. Zhang, D. L. Watkins, J. P. Mudrick, W. Cao, R. Bou Zerdan, A. J. Quartararo, I. Ghiviriga, J. Xue and R. K. Castellano, *J. Mater. Chem. A*, 2014, **2**, 1541–1549.
33 B. M. Schulze, D. L. Watkins, J. Zhang, I. Ghiviriga and R. K. Castellano, *Org. Biomol. Chem.*, 2014, **12**, 7932–7936.
34 X. Zhao, D. L. Watkins, J. F. Galindo, N. T. Shewmon, A. E. Roitberg, J. Xue, R. K. Castellano and S. S. Perry, *Org. Electron.*, 2015, **19**, 61–69.
35 N. T. Shewmon, D. L. Watkins, J. F. Galindo, R. B. Zerdan, J. Chen, J. Keum, A. E. Roitberg, J. Xue and R. K. Castellano, *Adv. Funct. Mater.*, 2015, **25**, 5166–5177.
36 G.-J. Zhao and K.-L. Han, *Acc. Chem. Res.*, 2012, **45**, 404.
37 A. P. Kulkarni, Y. Zhu and S. A. Jenekhe, *Macromolecules*, 2005, **38**, 1553–1563.
38 D. Gedefaw, M. Prosa, M. Bolognesi, M. Seri and M. R. Andersson, *Adv. Energy Mater.*, 2017, **7**, 1700575.
39 G. K. Dutta and S. Patil, *Org. Electron.*, 2012, **13**, 1266–1276.
40 Y. Cui, Y. Xu, H. Yao, P. Bi, L. Hong, J. Zhang, Y. Zu, T. Zhang, J. Qin, J. Ren, Z. Chen, C. He, X. Hao, Z. Wei and J. Hou, *Adv. Mater.*, 2021, **33**, 2102420.
41 S. Dailey, W. J. Feast, R. J. Peace, I. C. Sage, S. Till and E. L. Wood, *J. Mater. Chem.*, 2001, **11**, 2238–2243.
42 J. Hou, M.-H. Park, S. Zhang, Y. Yao, L.-M. Chen, J.-H. Li and Y. Yang, *Macromolecules*, 2008, **41**, 6012–6018.
43 H. You, H. Kang, D. Kim, J. S. Park, J.-W. Lee, S. Lee, F. S. Kim and B. J. Kim, *ChemSusChem*, 2021, **14**, 3520–3527.
44 J. Yuan, J. Ouyang, V. Cimrová, M. Leclerc, A. Najari and Y. Zou, *J. Mater. Chem. C*, 2017, **5**, 1858–1879.
45 K. R. Justin Thomas, M. Velusamy, J. T. Lin, C.-H. Chuen and Y.-T. Tao, *Chem. Mater.*, 2005, **17**, 1860–1866.
46 D. N. Kanekar, S. Chacko and R. M. Kamble, *Dyes Pigm.*, 2019, **167**, 36–50.
47 A. Tang, C. Zhan and J. Yao, *Chem. Mater.*, 2015, **27**, 4719–4730.
48 H. D. Kim, H. Ohkita, H. Benten and S. Ito, *ACS Appl. Mater. Interfaces*, 2014, **6**, 17551–17555.
49 C. Cui and Y. Li, *Energy Environ. Sci.*, 2019, **12**, 3225–3246.
50 T. Hasegawa, M. Ashizawa, S. Kawauchi, H. Masunaga, N. Ohta and H. Matsumoto, *RSC Adv.*, 2019, **9**, 10807–10813.
51 J. A. Elvidge and A. P. Redman, *J. Chem. Soc.*, 1960, 1710–1714.
52 N. A. Burton, D. V. S. Green, I. H. Millier, P. J. Taylor, M. A. Vincent and S. Woodcock, *J. Chem. Soc., Perkin Trans. 2*, 1993, 331–335.
53 J. M. Park, C. Y. Jung, Y. Wang, H. D. Choi, S. J. Park, P. Ou, W.-D. Jang and J. Y. Jaung, *Electrochim. Acta*, 2019, **298**, 650–662.
54 M. G. Cowan, R. G. Miller and S. Brooker, *Supramol. Chem.*, 2015, **27**, 780–786.
55 A. Saidykhan, N. W. Fenwick, R. D. Bowen, R. Telford and C. C. Seaton, *CrystEngComm*, 2021, **23**, 7108–7117.
56 S. Boothroyd, A. Kerridge, A. Broo, D. Buttar and J. Anwar, *Cryst. Growth Des.*, 2018, **18**, 1903–1908.
57 T. Hasegawa, K. Aoyagi, M. Ashizawa, Y. Konosu, S. Kawauchi, N. S. Sariciftci and H. Matsumoto, *Chem. Lett.*, 2015, **44**, 1128–1130.
58 M. Velusamy, J.-H. Huang, Y.-C. Hsu, H.-H. Chou, K.-C. Ho, P.-L. Wu, W.-H. Chang, J. T. Lin and C.-W. Chu, *Org. Lett.*, 2009, **11**, 4898–4901.

59 I. González, D. Cortés-Arriagada, P. Dreyse, L. Sanhueza, I. Crivelli, H. M. Ngo, I. Ledoux-Rak, A. Toro-Labbe, J. Maze and B. Loeb, *Polyhedron*, 2020, **187**, 114679.
60 M. S. Deshmukh and N. Sekar, *Dyes Pigm.*, 2015, **117**, 49–60.
61 V. Martínez-Martínez, J. Lim, J. Bañuelos, I. López-Arbeloa and O. Š. Miljanić, *Phys. Chem. Chem. Phys.*, 2013, **15**, 18023–18029.
62 E. Sucre-Rosales, R. Fernández-Terán, N. Urdaneta, F. E. Hernández and L. Echevarria, *Chem. Phys.*, 2020, **537**, 110854.
63 G. Qian, B. Dai, M. Luo, D. Yu, J. Zhan, Z. Zhang, D. Ma and Z. Y. Wang, *Chem. Mater.*, 2008, **20**, 6208–6216.
64 A. Khasbaatar, Z. Xu, J.-H. Lee, G. Campillo-Alvarado, C. Hwang, B. N. Onusaitis and Y. Diao, *Chem. Rev.*, 2023, **123**, 8395–8487.
65 W. T. Gallonde, C. Poidevin, F. Houard, E. Caytan, V. Dorcet, A. Fihey, K. Bernot, S. Rigaut and O. Galangau, *Angew. Chem., Int. Ed.*, 2023, e202313696.
66 A. Sánchez-Coronilla, M. Balón, M. A. Muñoz, J. Hidalgo and C. Carmona, *Chem. Phys.*, 2008, **351**, 27–32.
67 X. Liu, J. M. Cole and Z. Xu, *J. Phys. Chem. C*, 2017, **121**, 13274–13279.
68 M. Kubista, R. Sjöback, S. Eriksson and B. Albinsson, *Analyst*, 1994, **119**, 417–419.
69 G. Fu, T. Wang, J. Cai, J. Shi, Z. Luo, G. Li, X. Li, Z. Zhang and S. Yang, *Org. Electron.*, 2015, **18**, 70–76.
70 W. R. Erwin, C. Hungerford, H. F. Zarick, E. M. Talbert, P. Arora and R. Bardhan, *ACS Omega*, 2016, **1**, 722–729.
71 C. Deibel, T. Strobel and V. Dyakonov, *Adv. Mater.*, 2010, **22**, 4097–4111.
72 L. Yu, D. Qian, S. Marina, F. A. A. Nugroho, A. Sharma, S. Hultmark, A. I. Hofmann, R. Kroon, J. Benduhn, D.-M. Smilgies, K. Vandewal, M. R. Andersson, C. Langhammer, J. Martín, F. Gao and C. Müller, *ACS Appl. Mater. Interfaces*, 2019, **11**, 21766–21774.